Kim, K.-C., Shprits, Y. (2017): Dependence of the amplitude of magnetosonic waves on the solar wind and AE index using Van Allen Probes. - *Journal of Geophysical Research*, *122*, 6, pp. 6022—6034.

DOI: http://doi.org/10.1002/2017JA024094

AGU PUBLICATIONS

JGR

Journal of Geophysical Research: Space Physics

RESEARCH ARTICLE
10.1002/2017JA024094

Key Points:
- We present the dependence of the magnetosonic wave amplitudes both outside and inside the plasmapause on the solar wind and *AE* index
- Southward IMF B_z is the most influential parameter that affects the dayside wave amplitudes both outside and inside the plasmapause
- Solar wind number density contributes to enhancing the duskside waves outside the plasmapause

Correspondence to:
K.-C. Kim,
kyungchan80@gmail.com

Citation:
Kim, K.-C., and Y. Shprits (2017), Dependence of the amplitude of magnetosonic waves on the solar wind and *AE* index using Van Allen Probes, *J. Geophys. Res. Space Physics*, *122*, 6022–6034, doi:10.1002/2017JA024094.

Received 27 FEB 2017
Accepted 16 MAY 2017
Accepted article online 18 MAY 2017
Published online 5 JUN 2017

Dependence of the amplitude of magnetosonic waves on the solar wind and *AE* index using Van Allen Probes

Kyung-Chan Kim[1] **and Yuri Shprits**[2,3,4]

[1]Division of Science Education, College of Education, Daegu University, Gyeongsan, South Korea, [2]Helmholtz Centre Potsdam, GFZ German Research Centre for Geosciences, Potsdam, Germany, [3]Institute of Physics and Astronomy, University of Potsdam, Potsdam, Germany, [4]Department of Earth, Planetary, and Space Sciences, University of California, Los Angeles, California, USA

Abstract We present the dependence of the magnetosonic wave amplitudes both outside and inside the plasmapause on the solar wind and *AE* index using Van Allen Probe-A spacecraft during the time period of 1 October 2012 to 31 December 2015, based on a correlation and regression analysis. Solar wind parameters considered are the southward interplanetary magnetic field (IMF B_S), solar wind number density (N_{SW}), and bulk speed (V_{SW}). We find that the wave amplitudes outside (inside) the plasmapause are well correlated with the preceding *AE*, IMF B_S, and N_{SW} with time delays, each corresponding to 2–3 h (3–4 h), 4–5 h (3–4 h), and 2–3 h (8–9 h), while the correlation with V_{SW} is ambiguous both inside and outside the plasmapause. As measured by the correlation coefficient, the IMF B_S is the most influential solar wind parameter that affects the dayside wave amplitudes both outside and inside the plasmapause, while N_{SW} contributes to enhancing the duskside waves outside the plasmapause. The *AE* effect on wave amplitudes is comparable to that of IMF B_S. More interestingly, regression with time histories of the solar wind parameters and the *AE* index preceding the wave measurements outside the plasmapause shows significant dependence on the IMF B_S, N_{SW}, and *AE*: the region of peak coefficients is changed with time delay for IMF B_S and *AE*, while isolated peaks around duskside remain gradually decrease with time for N_{SW}. In addition, the regression with magnetosonic waves inside the plasmapause shows high coefficients around prenoon sector with preceding IMF B_S and V_{SW}.

1. Introduction

The spatial distribution and properties of magnetosonic waves (also named equatorial noise) in the Earth's magnetosphere have recently been studied intensively [e.g., *Santolík et al.*, 2004; *Shprits et al.*, 2013; *Tsurutani et al.*, 2014] due to the possibility that the waves may contribute to the acceleration of energetic electrons that could be acting as a source population for the outer electron radiation belt [e.g., *Horne et al.*, 2007], to the scattering of energetic protons that cause proton aurora on the dayside [e.g., *Xiao et al.*, 2014], or to the bounce resonance scattering of energetic electrons [e.g., *Shprits*, 2016]. Magnetosonic waves are whistler mode emissions occurring at frequencies between the proton cyclotron frequency (f_{cp}) and the lower hybrid resonance frequency (f_{LHR}), and propagate nearly perpendicular to the background magnetic field. They are present both outside and inside the plasmapause, and intense magnetosonic waves are distributed mostly on the dayside within a few degrees of the magnetic equator [*Russell et al.*, 1970; *Laakso et al.*, 1990; *Kasahara et al.*, 1994; *Santolík et al.*, 2002; *Meredith et al.*, 2008; *Ma et al.*, 2013; *Hrbáčková et al.*, 2015]. A recent study has observed a very rare case of magnetosonic waves off the magnetic equator [*Zhima et al.*, 2015]. It is known that a ring distribution of ~10 keV protons injected during geomagnetically disturbed times can provide a source of free energy for exciting magnetosonic waves [*Perraut et al.*, 1982; *Curtis and Wu*, 1979; *Boardsen et al.*, 1992; *Horne et al.*, 2000; *Chen et al.*, 2010, 2011; *Ma et al.*, 2014; *Balikhin et al.*, 2015]. Previous studies therefore have focused on the geomagnetic activity dependence of spatial distribution of wave amplitudes and have shown that the waves are enhanced with increasing geomagnetic activity [e.g., *Meredith et al.*, 2008; *Ma et al.*, 2013; *Hrbáčková et al.*, 2015].

A recent study of *Kim and Chen* [2016] developed a model that presents the spatial and temporal evolution of the amplitudes of magnetosonic wave response to the variation in solar wind during the storm times. They suggest that southward interplanetary magnetic field (IMF) B_z is closely correlated with the wave amplitudes both outside and inside the plasmapause, and the solar wind dynamic pressure is effective in enhancing

wave amplitudes locally around the postnoon sector outside the plasmapause. The role of dynamic pressure on exciting magnetosonic waves is not well studied. Their study was based on measurements of the Time History of Events and Macroscale Interactions during Substorms (THEMIS) spacecraft, which provides two components of the magnetic and electric wave spectral density, i.e., perpendicular and parallel to the spin axis that is roughly aligned to the local magnetic field with an angle of $<11°$ [*Cully et al.*, 2008]. From cold plasma theory [*Stix*, 1992], they identified magnetosonic wave signals based only on the ratio of the magnetic and electric field components of the wave spectra without taking into account the wave polarization properties such as wave normal angle, ellipticity, and planarity. In addition, a ratio of two electric field components used for identification of magnetosonic waves was applied to only one fifth of approximately 4.5 years of data (1 May 2010 to 30 November 2014) used in their study since the ratio has been unavailable since March 2011. Their database of wave emissions therefore might also contain other emissions than magnetosonic waves, mostly plasmaspheric hiss inside the plasmapause. In this study, we reanalyze the spatial and temporal dependences of wave amplitudes on the solar wind and *AE* index using NASA's Van Allen Probes by identifying wave signals based on the wave polarization properties and investigate whether the result is still valid.

The remainder of this paper is organized as follows. The methodology that captures highly oblique magnetosonic waves from Van Allen Probe-A is described in section 2, the correlation analysis results between magnetosonic wave amplitudes and the solar wind parameters as well as *AE* index are presented in section 3, the global distribution of wave amplitude in terms of solar wind parameters and *AE* index is presented in section 4, the linear regression analysis results are presented in section 5, and the summary and conclusions are presented in section 6.

2. Van Allen Probe Observations of Magnetosonic Waves

The twin Van Allen Probes orbit at an altitude of 600–30,000 km in near-equatorial elliptical orbit. The Electric and Magnetic Field Instrument Suite and Integrated Science (EMFISIS) instrumentation suite provides the DC magnetic fields and wave electric and magnetic fields. The EMFISIS/Waves instrument includes a six-channel Waveform Receiver (WFR), which measures wave spectra from 10 Hz to 12 kHz for all the three components of both magnetic and electric fields, and a single-channel High-Frequency Receiver (HFR), which measures a single electric component of waves between 10 kHz and 400 kHz. Using the singular value decomposition method [*Santolík et al.*, 2003], we identify the magnetosonic wave signal satisfying the magnetosonic wave conditions of wave normal angle $\geq 80°$ and the absolute value of wave ellipticity ≤ 0.2 from EMFISIS WFR data. For this work, we first remove spectral density less than twice the background level, defined by the median value of spectral density for each frequency throughout 1 day. The wave spectral density measured by EMFISIS HFR is used to identify the plasmapause's location. High intensity of electrostatic electron-cyclotron harmonic waves is usually observed outside the plasmapause [*Meredith et al.*, 2004]. The low-density regions outside the plasmapause are thus determined per half orbit when the root-mean-square wave amplitudes integrated over the frequency range between $2.5f_{ce}$ (f_{ce} is the electron gyrofrequency) and $5.0\ f_{ce}$ suddenly increase using HFR data with the background removed. In addition, the appearance and disappearance of the whistler mode chorus between $0.1f_{ce}$ and $0.8f_{ce}$ and plasmaspheric hiss between 40 Hz and 2 kHz are used to manually modify the plasmapause's location determined above.

Figure 1 shows an example of magnetosonic wave signals observed by Van Allen Probe-A on 6 October 2012. Shown, from top to bottom, are wave spectra of electric field from HFR (Figure 1a), wave spectra of magnetic and electric field from WFR (Figures 1b and 1c), wave normal angle (Figure 1d), planarity (Figure 1e), signed ellipticity (Figure 1f), Poynting vector direction (Figure 1g), and wave flag (Figure 1h). The crossings of plasmapause determined by the HFR wave spectra are indicated by black vertical lines. Different curves in each figure except for Figure 1a correspond to, from top to bottom, f_{ce}, $0.5f_{ce}$, $0.1f_{ce}$, f_{LHR}, $0.5f_{\mathrm{LHR}}$, and f_{cp}, respectively. Different curves in Figure 1a indicate harmonics of f_{ce} up to $5.0f_{ce}$. From Figures 1d to 1h, only signals with the background removed are displayed. In Figure 1h, wave spectral densities satisfying the above criteria of magnetosonic waves are indicated with different colors for regions outside and inside the plasmapause. The selected signals are clearly distinguished from other types of waves such as whistler mode chorus outside the plasmapause and plasmaspheric hiss inside the plasmapause. In this study, we identified magnetosonic wave signals made from measurements during the time period of 1 October 2012 to 31 December 2015 using the Van Allen Probe-A spacecraft only to avoid double counting magnetosonic wave

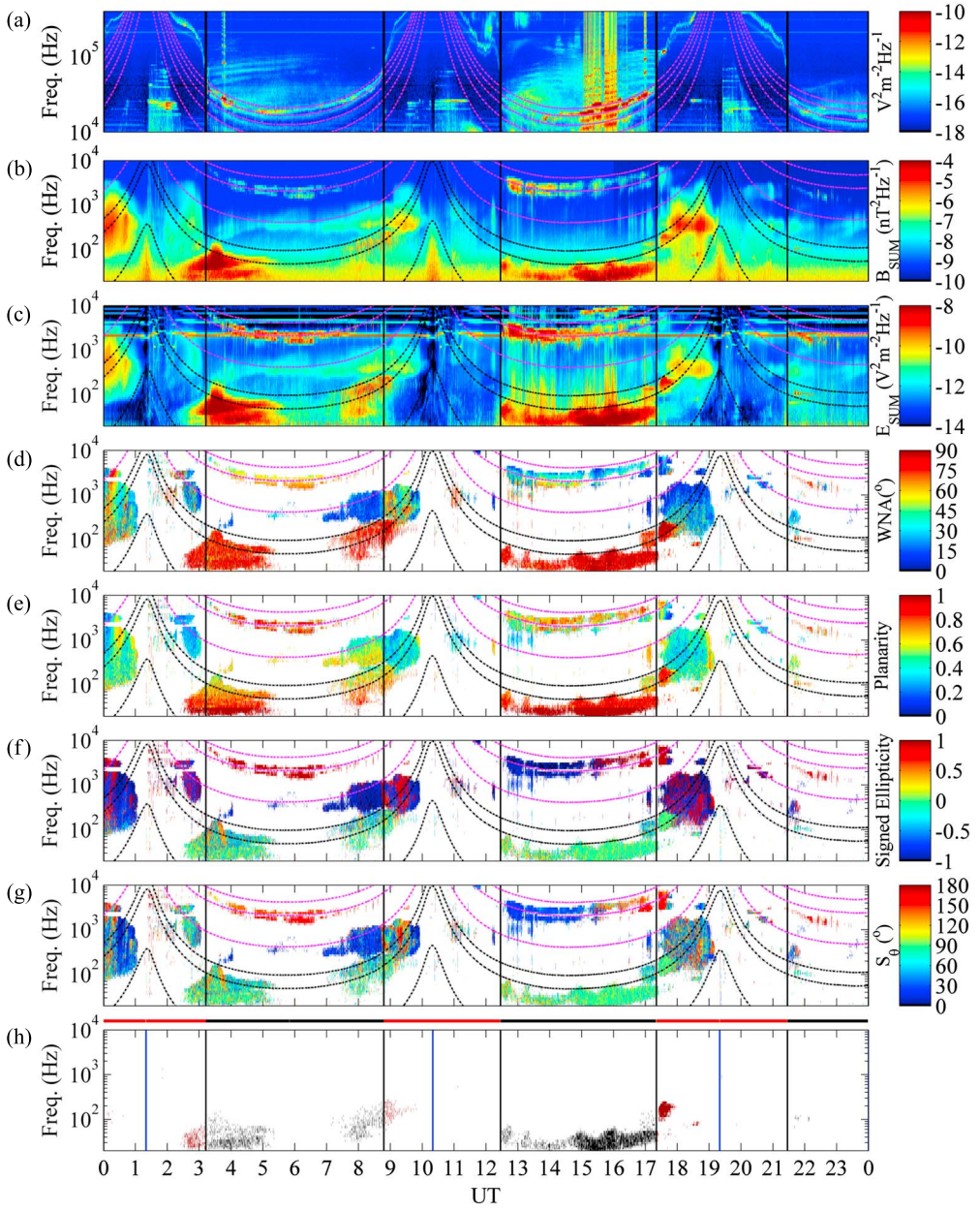

Figure 1. An example of magnetosonic waves observed on Van Allen Probe-A on 6 October 2012. From top to bottom, the panels, respectively, correspond to (a) wave electric intensity spectrograms measured by HFR, (b and c) magnetic and electric wave spectra measured by WFR, (d) wave normal angle (deg), (e) planarity, (f) signed ellipticity, (g) Poynting vector direction (deg), and (h) wave flag. The vertical black lines indicate the plasmapause location for each half orbit. In Figure 1h, the regions outside and inside the plasmapause are distinguished by horizontal black and red lines, respectively, and magnetosonic wave signals in each region are also indicated with the corresponding color. The vertical blue lines show the perigee time of each orbit.

events when binning data and calculated the root-mean-square amplitude (B_W) of the magnetosonic wave by integrating over the frequency range between f_{cp} and f_{LHR} from magnetic wave spectra as shown in Figure 1b.

Figure 2 presents the average magnetosonic wave amplitudes as a function of L value and magnetic local time (MLT) outside (Figure 2, top row) and inside (Figure 2, bottom row) the plasmapause, and for equatorial (Figure 2, left column) and off-equatorial (Figure 2, right column) regions, divided by 5° of magnetic latitude (MLAT), at a resolution of 0.2 R_E in L value and 1 h in MLT. The L value in this study is the *McIlwain* L [*McIlwain*, 1961] of locally mirroring particles based on the TS04D [*Tsyganenko and Sitnov*, 2005] magnetic field. The

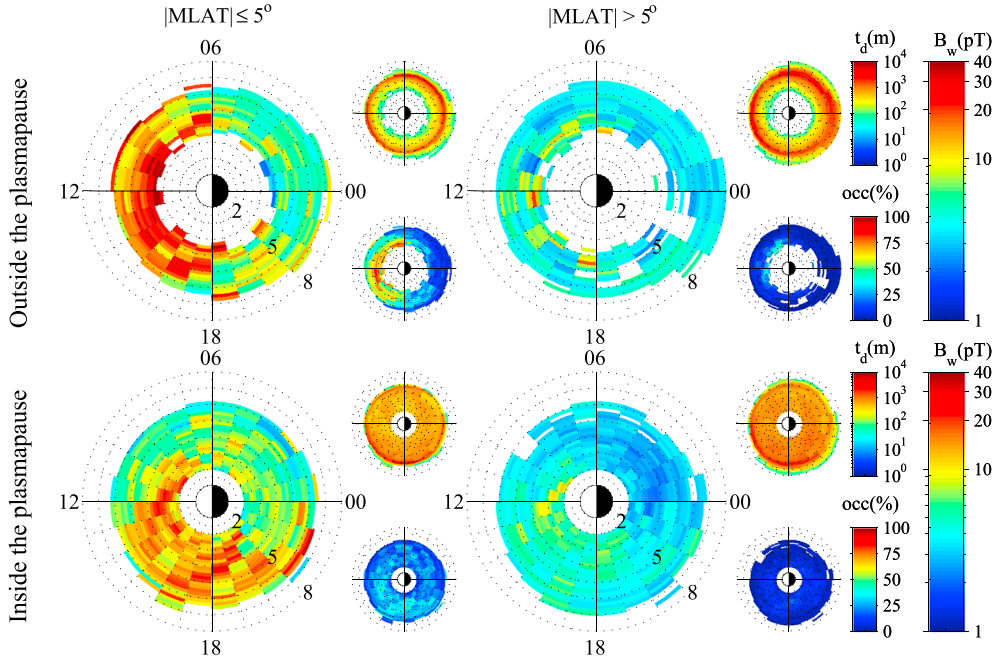

Figure 2. The global distributions of the average magnetosonic wave amplitude from 1 October 2012 to 31 December 2015 for locations (top row) outside and (bottom row) inside the plasmapause in the (left column) equatorial and (right column) nonequatorial regions. Average wave amplitudes are shown in the large panels and the corresponding dwell time of spacecraft and occurrence rates in the top and bottom small plots, respectively.

corresponding occurrence rates, which are defined as the ratio (in percentage) of wave observation time to dwelling time of spacecraft in each bin of L, MLT, and MLAT, and the dwelling time (in minute) are also shown in the bottom and top small plots, respectively. Note that the occurrence rate is only calculated when the time spacecraft spent in a given bin is larger than 1 h. Outside the plasmapause, the most intense waves are found mainly in the region $3.5 \leq L \leq 5$ from 6 to 18 MLT near the equator with the average amplitude of 20 ± 8 pT, showing 62(±11)% occurrence rate. The region of intense waves inside the plasmapause near the equator is shifted more toward the postnoon sector than outside with a relatively weak average amplitude of 13 ± 5 pT in the region $2 \leq L \leq 5$ from 9 to 21 MLT, showing 27(±7)% occurrence rate. The result indicates that magnetosonic wave amplitude is strongly dependent on MLT, both outside and inside the plasmapause. This is qualitatively consistent with the previous findings of the Van Allen Probes [*Ma et al.*, 2016], Cluster [*Hrbáčková et al.*, 2015], and THEMIS [*Ma et al.*, 2013; *Kim and Chen*, 2016].

3. Solar Wind Dependence of Magnetosonic Wave Amplitude: Correlation Coefficients

We now examine the relationship between variations in magnetosonic wave amplitude and solar wind parameters as well as *AE* index. The solar wind parameters considered are the southward IMF B_z (IMF B_S), defined by negative value of IMF B_z, and the solar wind number density (N_{SW}) and the bulk speed (V_{SW}). First, we correlate the 1 min averaged wave amplitudes with the maxima of solar wind parameters and *AE* index in a time window of 1 h, the center of which corresponds to the wave identification time. The spearman's Rank Order Correlation Coefficient (ROCC) is estimated based on wave amplitudes sorted in each 0.2 L and 6 MLT bin [*Press et al.*, 1992] by sliding the time window from 0 to 24 h backward, relative to the wave identification time. Only magnetosonic waves observed in the equatorial region less than 5° of magnetic equator are used to estimate the ROCC since high occurrence rate of waves is near the equator as shown in Figure 2.

Figure 3 presents the estimated correlation coefficients, ROCCs of magnetosonic wave amplitudes outside the plasmapause with each solar wind parameter, and *AE* index as a function of time shift (delay time) of 1 h time window and L value in four MLT sectors, a dawn (3–9 MLT), a noon (9–15 MLT), a dusk (15–21 MLT), and a midnight (21–3 MLT). The median value of all ROCCs across all L values for a given time shift is

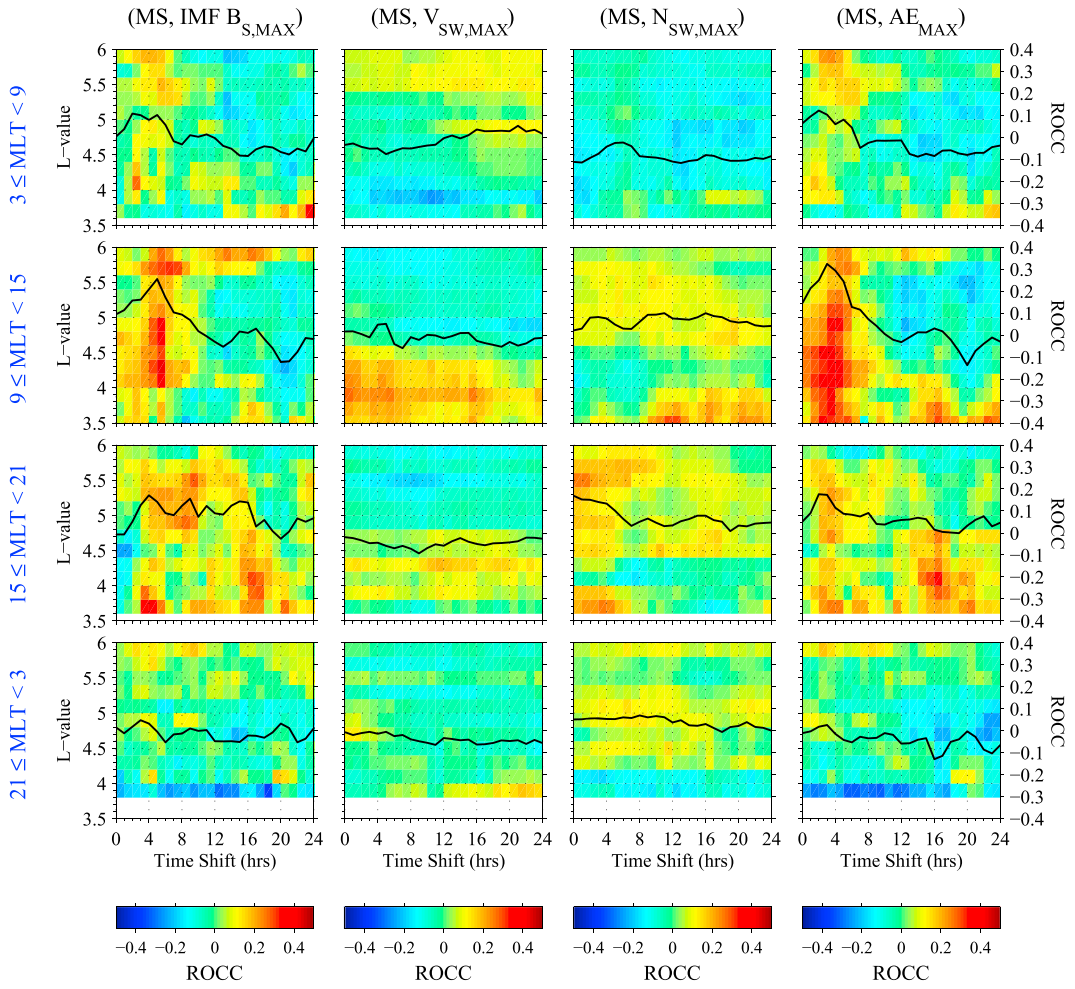

Figure 3. ROCC of magnetosonic wave amplitudes outside the plasmapause with solar wind parameters (IMF B_S, V_{SW}, and N_{SW}) and *AE* index as a function of time shift of a 1 h time window and L value for MLT locations, subdivided into four sectors, (first row) 3–9 MLT, (second row) 9–15 MLT, (third row) 15–21 MLT, and (fourth row) 21–3 MLT. The median value of all ROCCs across all L values for a given time shift is displayed together with a black solid line. The white region indicates the bins with sample number less than 250 counts.

overlaid in each figure with a black solid line, which allows for more intuitive interpretation of a relationship between the wave amplitude and each parameter. The best positive correlation between the IMF B_S and the wave amplitude can be found in the noon sector where local maxima are clearly seen at a time shift of 5 h for $4 < L < 5$, and other nearby peaks (but not too significant) are seen for $L > 5$. The maximum correlation reaches up to 0.42 around L ~ 4.3. The median ROCC correlation also shows a local maximum at a time shift of 5 h, and it tends to become weaker toward zero with negative values away from the peak time. However, such a pattern becomes less significant away from the noon sector and no significant peak is seen in the midnight sector. The correlation with IMF B_S indicates that dayside wave amplitude increases for most of L values at 5 h after the southward IMF B_z, which is likely related to the finite drift time of the injected ions associated with substorms. A similar feature is also evident in the correlation with the *AE* index, as shown in the last column but with a somewhat shorter delay time and a slightly higher correlation in the noon sector (see the median curve). The maximum correlation with *AE* reaches up to 0.4 at a delay time of 3 h in the noon sector around L ~ 4.1.

In contrast, the correlation between V_{SW} and wave amplitude is almost uniformly distributed over most of the L values and MLT sectors and can be either sign, depending on L values, but moderate local minima are also seen in the dawn and dusk sectors around L = 4 and L = 5.5, respectively. The median curves are almost flat with a relatively low coefficient, indicating no unambiguous correlation within a 24 h time window. It is also

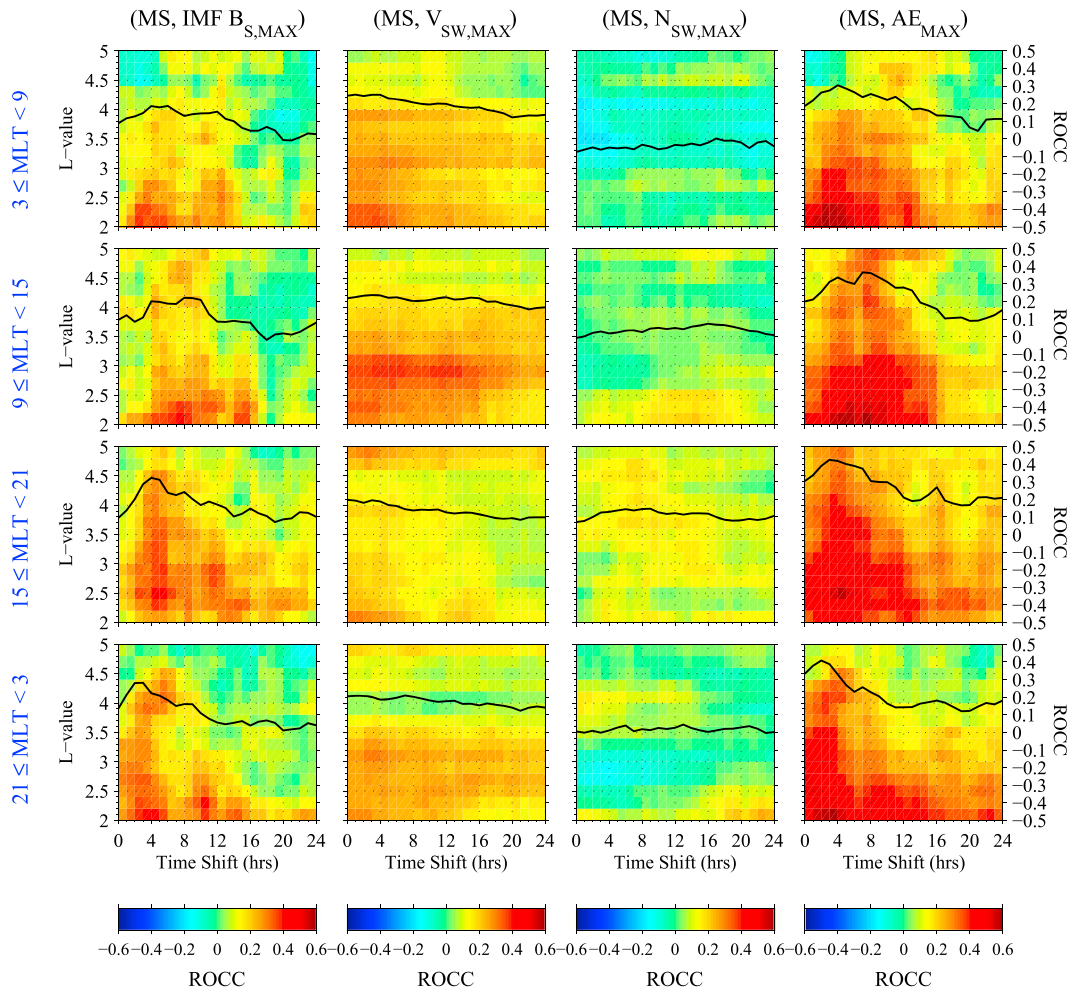

Figure 4. The same as in Figure 3 but correlated with magnetosonic wave amplitudes inside the plasmapause and different *y* axis scales on both sides of each panel.

found in the correlation with N_{SW} over all MLT sectors except for that in the dusk sector where the correlation shows peaks of ~0.25 at a time delay less than 4 h, shorter than that of any other parameter.

The correlations made from the wave amplitudes inside the plasmapause in four MLT sectors are presented in Figure 4. In the first column, an interesting feature for IMF B_S is that local maxima are seen at a shorter delay time for L $<$ 3 as MLT increases from noon to midnight, around 7 h in noon sector, around 4 h in dusk sector, and around 2 h in midnight sector. Local maxima of $>$0.35 with IMF B_S are also seen at a delay time of 3–5 h, depending on L values, for L $<$ 3 in the dawn sector, but the peaks are not significant compared to those in other sectors. The correlation with the *AE* index shown in the last column shows local maxima at a time delay of 2–4 h, depending on L value, for L $<$ 3 in the dawn sector, and they are at a shorter time delay as MLT increases from noon to midnight, a similar feature to that of IMF B_S, but with a quite higher correlation ($>$0.55) in the all sectors. The best correlation in the midnight sector is almost instantaneous, indicating that magnetosonic wave amplitudes increase simultaneously with the *AE* enhancements, and the high positive correlations in the all sectors persist for several hours. In contrast, the correlation with V_{SW} and N_{SW} shows that local peaks for both N_{SW} and V_{SW} are not pronounced compared to those of IMF B_s, which is also indicated by their median curves and that the median curves are overall flat with a time shift in the all sectors. The results in Figure 4 suggest that the IMF B_S is better correlated with variations in the wave amplitudes inside the plasmapause than any other solar wind parameters, and the correlation with both V_{SW} and N_{SW} is ambiguous. In section 5, we will present a more quantitative description of such a relationship between the solar wind and wave amplitude.

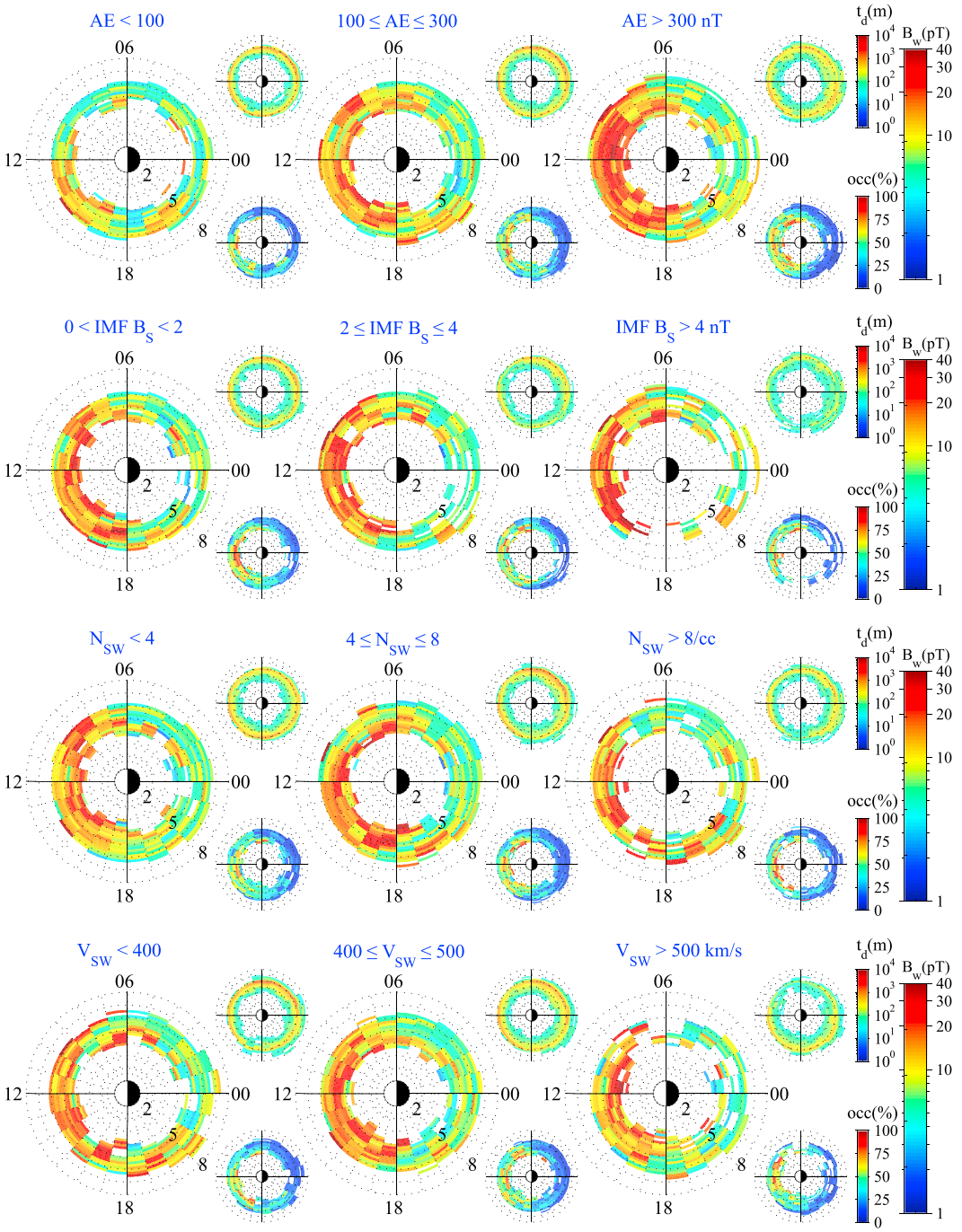

Figure 5. The average magnetosonic wave amplitude as a function of L and MLT for different activity levels of (first row) *AE* 2–3 h, (second row) IMF B_S 4–5 h, (third row) N_{SW} 2–3 h, and (fourth row) V_{SW} 6–7 h preceding the wave measurements. The white area represents the bins with dwell time less than 30 min in a given bin.

4. Global Distribution of Magnetosonic Wave Amplitude: Dependence on Solar Wind Parameters and *AE* Index

In this section, we present the spatial distribution of magnetosonic waves for both outside and inside the plasmapause as a function of activity levels of solar wind parameters and *AE* index. Figure 5 shows how the average wave amplitudes outside the plasmapause vary in MLT and L for three ranges of *AE* (Figure 5, first row): $AE < 100$, $100 \leq AE \leq 300$, and $AE > 300$ nT; for three ranges of IMF B_S (Figure 5, second row): $0 <$ IMF

$B_S < 2$, $2 \leq$ IMF $B_S \leq 4$, and IMF $B_S > 4$ nT; for three ranges of N_{SW} (Figure 5, third row): $N_{SW} < 4$, $4 \leq N_{SW} \leq 8$, and $N_{SW} > 8$/cc; and for three ranges of V_{SW} (Figure 5, fourth row): $V_{SW} < 400$, $400 \leq V_{SW} \leq 500$, and $V_{SW} > 500$ km/s, respectively. The corresponding occurrence rates and dwelling time of spacecraft in each bin are shown in the bottom and top small plots, respectively. The wave amplitudes are sorted by the maximum of each parameter at the delay time corresponding to the maximum correlation shown in the previous section based on median coefficients of dayside MLT sectors (6 to 18 MLT). The delay times are 2–3 h for *AE*, 4–5 h for IMF B_S, 2–3 h for N_{SW}, and 6–7 for V_{SW}, respectively. Note that the correlation with V_{SW} (N_{SW}) and wave amplitudes does not differ much within the 24 h time window.

From Figure 5 (first row), we can see that the wave amplitudes, mostly on the dayside, increase significantly with *AE*, and the average wave amplitudes in the region $3.5 \leq L \leq 5$ from 6 to 18 MLT are 10 pT, 15 pT, and 19 pT during low, moderate, and enhanced activities, respectively. The corresponding peak amplitudes are 22 pT, 32 pT, and 42 pT, respectively. However, such a trend cannot be easily seen among the solar wind parameters. First, the result for the IMF B_S (Figure 5, second row) shows that a modest increase in wave amplitude is seen mostly in the dayside under more southward IMF B_z. Next, the result with N_{SW} (Figure 5, third row) indicates that duskside waves significantly increase for the transition from $N_{SW} < 4$ to $4 \leq N_{SW} \leq 8$, while the dawn sector waves diminish for the transition from $4 \leq N_{SW} \leq 8$ to $N_{SW} > 8$. Lastly, the result with V_{SW} (Figure 5, fourth row) shows that the enhanced amplitudes are seen over the dayside ($9 <$ MLT < 18) for the transition from slow to moderate V_{SW}, and the region of intense waves is shifted toward the prenoon sector with a modest increase for the transition to high V_{SW}.

Figure 6 shows the spatial distribution of magnetosonic waves inside the plasmapause in the same format as in Figure 5, but the delay times are 3–4 h for *AE*, 3–4 h for IMF B_S, 8–9 h for N_{SW}, and 2–3 h for V_{SW}, all prior to magnetosonic wave measurements, which are obtained based on median coefficients of 9–21 MLT sector where the most intense waves are observed, as shown in Figure 2. Compared to Figure 5, a remarkable difference is that the waves around the postnoon sector (12–18 MLT) become intensified with increasing levels of all solar wind parameters and *AE* index, and active regions extend toward prenoon and premidnight sectors (though less clear for the transition from second level to last level of V_{SW} due to lack of data coverage).

More quantitatively, the average wave amplitudes in the region $2 \leq L \leq 5$ from 9 to 21 MLT in order of low to high level are 8, 12, and 18 pT for *AE*; 11, 16, and 21 pT for IMF B_S; 11, 13, and 15 pT for N_{SW}; and 10, 14, and 16 pT for V_{SW}, respectively. The corresponding peak amplitudes are 22, 24, and 31 pT for *AE*; 23, 35, and 40 pT for IMF B_S; 27, 25, and 35 pT for N_{SW}; and 18, 26, and 52 pT for V_{SW}, respectively.

5. Solar Wind Dependence of Magnetosonic Wave Amplitude: Regression Coefficients

The correlation analysis shown in section 3 is useful for estimating the degree of how closely the solar wind is related to the magnetosonic wave amplitude. However, some solar wind parameters can be mutually correlated. In order to quantify the independent contributions of solar wind parameters to the spatial and temporal variations of the wave amplitude, we use a linear regression analysis [e.g., *Draper and Smith*, 1998], which is useful for isolating the role of one variable from all of the others in the model. In our analysis, the independent variables are IMF B_S, and the logarithm of N_{SW} and V_{SW}, and the dependent variable is the logarithm of wave amplitude (B_W). All variables are normalized to fall between -1 and 1 by using the following equation: $X_{n,i} = 2 \times (X_i - \min(X))/(\max(X) - \min(X)) - 1$ where X is an $n \times 1$ column vector of n samples of each variable, i.e., $X = (X_1, X_2, \ldots, X_n)$ and $X_{n,i}$ are ith normalized data. The notation $\max(X)$ (or $\min(X)$) indicates the maximum (or minimum) of X. The assumed linear relationship between independent and dependent variables for the analysis is as follows:

$$\log_{10} B_W = C_{0,SW} + C_{N_{SW}} \log_{10} N_{SW} + C_{V_{SW}} \log_{10} V_{SW} + C_{\text{IMF } B_S} \text{IMF } B_S \quad (1)$$

where $C_{0,SW}$ is intercept and $C_{N_{SW}}$, $C_{V_{SW}}$, and $C_{\text{IMF } B_S}$ are slope with respect to N_{SW}, and V_{SW}, IMF B_S, respectively. The parameters are determined in each 1 L and 3 MLT bin by a traditional least squares solution. For dependent variables, we use the instantaneous value of each solar wind measurement and the *AE* index as well as their values prior to the time of the magnetosonic wave measurements. Regression analysis with

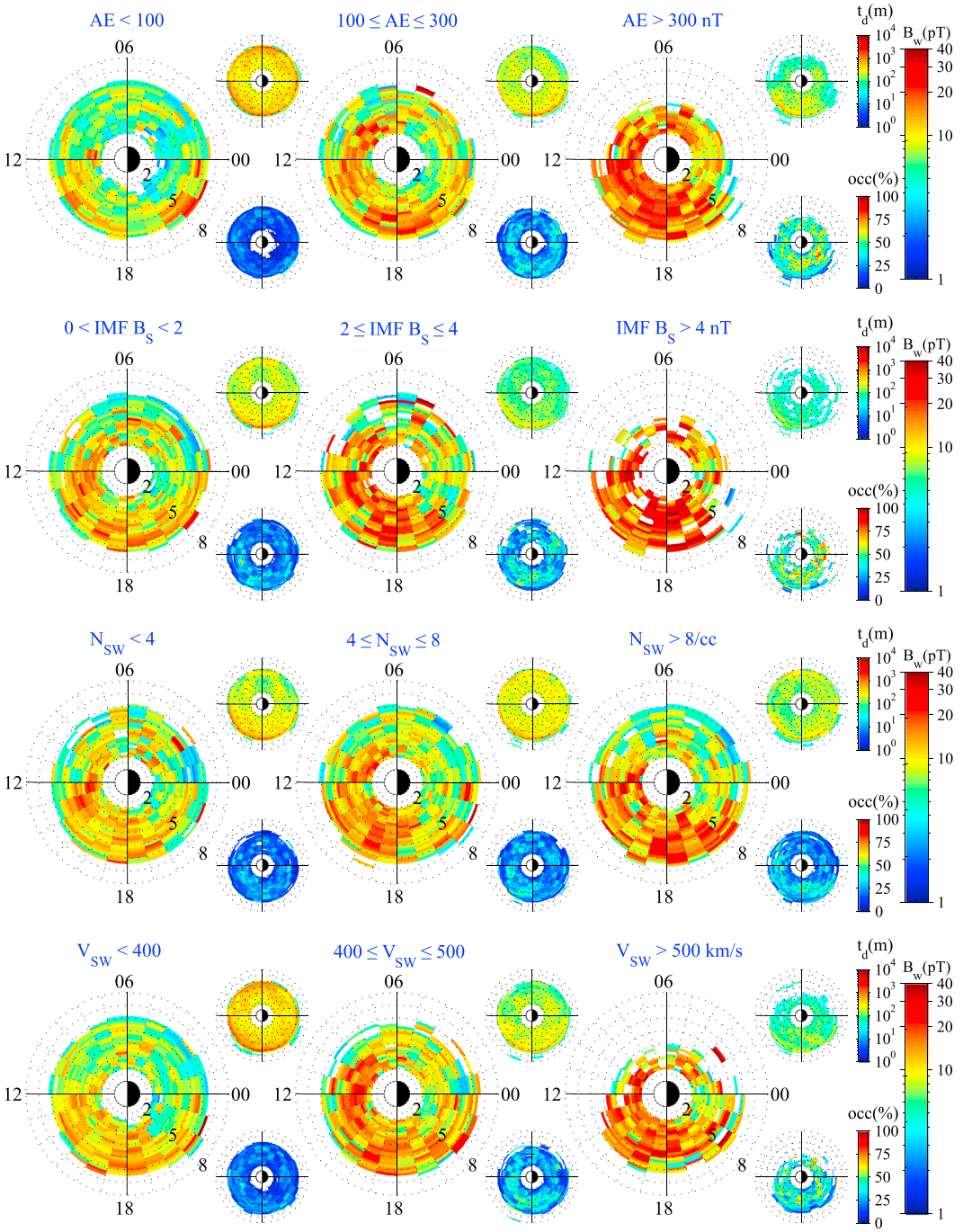

Figure 6. The same as in Figure 5 but with the magnetosonic wave amplitude inside the plasmapause and (first and second rows) *AE* 3–4 h and IMF B_S 3–4 h and (third and fourth rows) N_{SW} 8–9 h and V_{SW} 2–3 h preceding the wave measurements.

preceding solar wind conditions and geomagnetic activities will give insight into the time behavior of magnetosonic wave.

Figure 7 summarizes the results of regression analysis between the solar wind parameters and the wave amplitudes outside the plasmapause. In the last column, we also present the results of regression analysis with the *AE* index, which we simply assumed as $\log_{10}B_W = C_{0,AE} + C_{AE}\log_{10}AE$. Each panel shows the color-coded value of the regression coefficient. Figure 7 (first row) uses the instantaneous value of each dependent parameter. It is evident that the regions of particularly high positive coefficients differ among solar wind

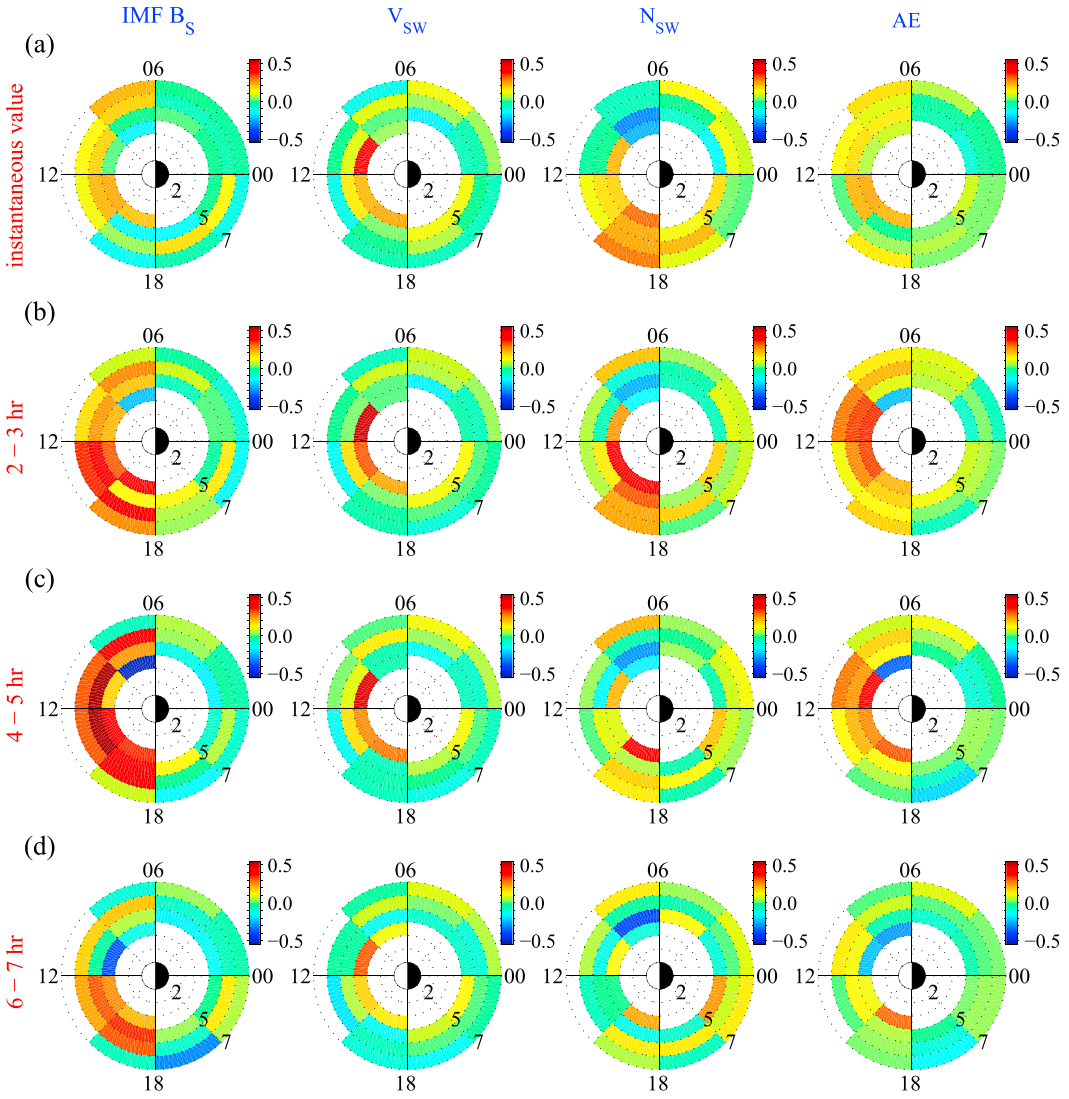

Figure 7. L-MLT dial plot of regression coefficients defined in equation (1) between magnetosonic wave amplitudes outside the plasmapause and solar wind parameters and *AE* index. Comparison is made among (a) instantaneous value, (b) 2–3 h ago, (c) 4–5 h, and (d) 6–7 h ago of dependent variables relative to wave measurements.

parameters: postnoon and dawn sector for IMF B_S, noon sector for V_{SW}, and the dusk sector for N_{SW}. This clearly suggests the spatial dependence of magnetosonic waves on solar wind parameters and also agrees well with the results of the correlation analysis noted in section 3. The regression with the *AE* index shows a similar spatial pattern as that of IMF B_S.

The results of regressions with the time-delayed solar wind parameters and *AE* index are shown in Figures 7b–7d, respectively, for 2–3 h, 4–5 h, and 6–7 h prior to the wave identification time. We find, from the regression with IMF B_S, that the regions of particularly high positive coefficient change significantly with time, around 12–18 MLT in the previous 6 to 7 h, 9–15 MLT in the previous 4 to 5 h, 12–18 MLT in the previous 2 to 3 h, and the postnoon and dawn sectors in the instantaneous time. This suggests that the combined effect of time histories of IMF B_S makes it possible to accurately estimate the variation in wave amplitudes over the entire dayside, where the most intense waves are present, as shown in Figure 2, when we model the observed wave amplitude. In other words, there would be a missing portion when using only one time history in modeling the observed wave amplitude. The largest coefficient among all the time histories is found on the dayside at 4–5 h, which indicates the best response time of magnetosonic wave amplitudes to the variation in solar wind. The time may be related to the finite drift time of energetic ion particles, which is known as a source

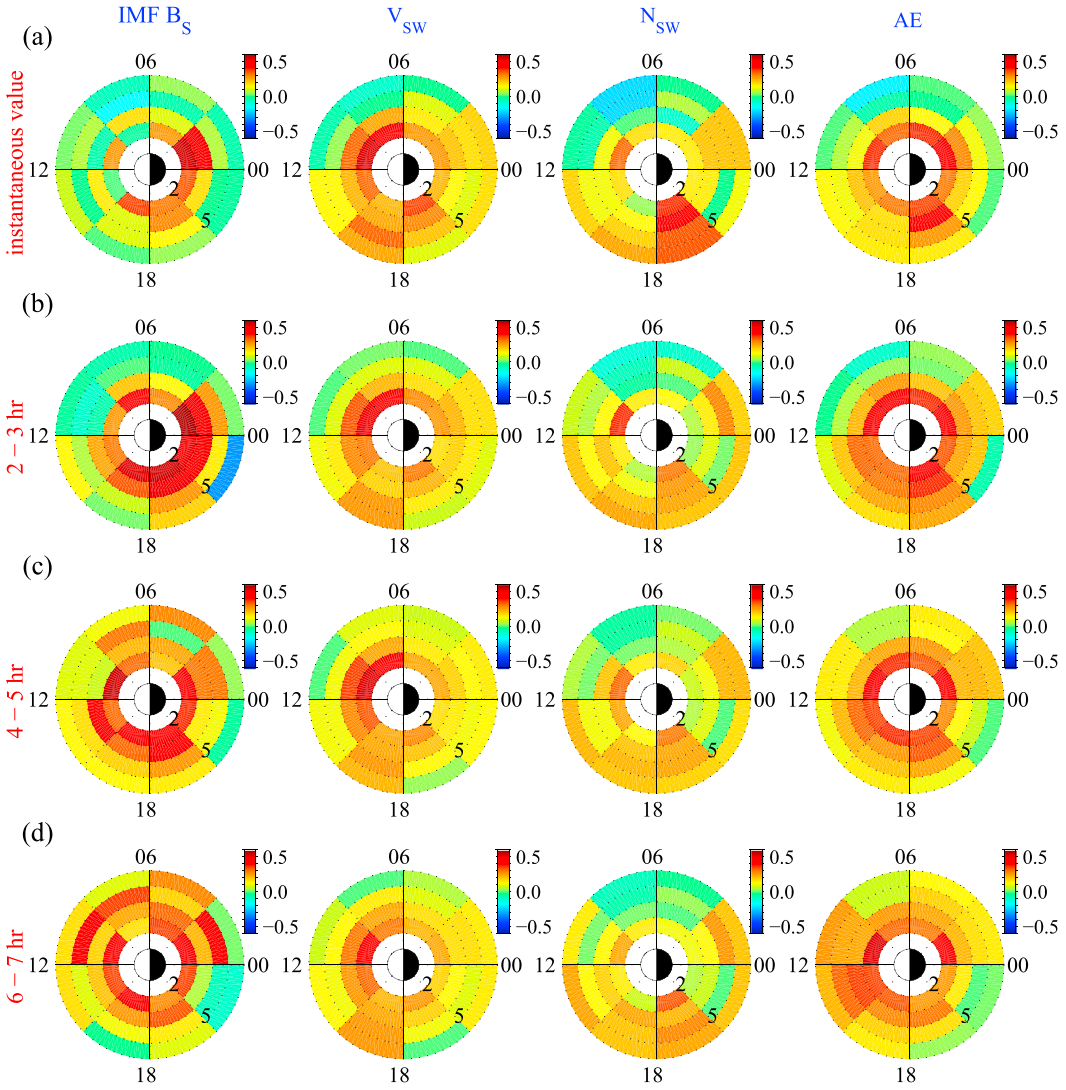

Figure 8. The same as Figure 7 but with regression coefficient with magnetosonic wave amplitude inside the plasmapause.

population of existing magnetosonic waves, as shown in section 3. A similar spatial pattern is seen in the result of regression with *AE* for all the times except for 2–3 h where the region of peak coefficients is shifted more toward the prenoon sector than IMF B_S. In contrast, the coefficients for V_{SW} remain to be low with time except for $3 \leq L < 4$ around noon sector and those for N_{SW} around 18 MLT gradually decrease with time, indicating that N_{SW} may contribute to local enhancement of wave amplitude around the dusk side.

A summary of regression coefficients derived from wave amplitudes inside the plasmapause is presented in Figure 8, plotted in the same format as in Figure 7. There are a few notable features in the plots. First, regression with time histories of IMF B_S indicates that the spatial distribution of coefficients significantly changes with time delay. In the previous 6–7 h, the region of high positive coefficients is located around prenoon sector, while it is located in the dusk sector and premidnight sector, each in the previous 4–5 h and 2–3 h. Second, regression with V_{SW} indicates that positive high coefficients around 6–12 MLT for $L < 4$ and 15–18 MLT for $L \geq 4$ appear significantly for all the times. The regression with N_{SW} also shows high coefficients around prenoon and dusk sector for all the times. Third, regression with *AE* index shows a significant change of spatial distribution of coefficients, the region of high positive coefficient shifts from around noon sector in the previous 4–5 and 6–7 h to around premidnight in the previous 2–3 and instantaneous time. The results in Figure 8 suggest that wave amplitudes inside the plasmapause are enhanced around the prenoon sector after enhancements in all of solar wind parameters, though the delay time slightly differs among them,

which is consistent with the result that the enhanced wave amplitudes around prenoon sector appear during active times, as shown in Figure 6. Interestingly, the region is consistent with that of intense waves outside the plasmapause, as shown in Figure 2, and we thus expect that magnetosonic waves may penetrate into the plasmasphere through the prenoon sector during active times and become the source of waves in the plasmasphere. Another possibility that one might raise for the prenoon waves is waves in the plasmaspheric plumes. In this study, we have not distinguished between wave amplitudes inside and outside the plasmaspheric plumes. These will be further investigated in future studies.

6. Summary and Conclusions

In this study we have presented the solar wind and geomagnetic activity dependence of magnetosonic wave amplitude, identified based on the wave polarization properties from Van Allen Probe-A measurements during the time period of 1 October 2012 to 31 December 2015, for both outside and inside the plasmapause. Our main conclusions on the statistical data analysis are summarized as follows:

1. The most intense waves are distributed on the dayside in the equatorial region both outside and inside the plasmapause, and their MLT region inside the plasmapause is skewed more toward the dusk sector than outside.
2. The delay times of magnetosonic wave activation outside (inside) the plasmapause in response to the solar wind and geomagnetic activity differ among them: they are 2–3 h (3–4 h) for *AE* and 4–5 h (3–4 h) for IMF B_S, all prior to the wave measurements when based on median coefficients of 6–18 MLT sector (9–21 MLT). The delay times for IMF B_S and *AE* suggest that wave activation is likely related to the ion drift injected during active times.
3. Of the solar wind parameters considered, IMF B_S is the most influential parameter that affects the dayside wave amplitudes both outside and inside the plasmapause, followed by N_{SW} that is contributing to enhancing the duskside wave outside the plasmapause.
4. Magnetosonic wave activity is monotonically amplified on the dayside (postnoon sector), outside (inside) the plasmapause with increasing *AE*. In contrast, the intense wave region outside the plasmapause differs with increasing levels of solar wind parameters, although inside the plasmapause remains unchanged among the parameters.
5. Regression with time histories of IMF B_S and N_{SW} preceding wave measurements outside the plasmapause shows that the region of particularly high coefficients for IMF B_S is changed with time on the dayside and coefficients for N_{SW} around dusk sector gradually decrease with time.
6. Regression with time histories of IMF B_S and V_{SW} preceding wave measurements inside the plasmapause shows high regression coefficients around the prenoon sector inside the plasmapause, implying the source region of waves inside the plasmapause.

Similar to the study of *Kim and Chen* [2016], we also estimated a reasonable delay time of magnetosonic wave activation outside the plasmapause to the solar wind and *AE* index, which supports the excitation of magnetosonic waves by a ring distribution of ion population. However, some differences exist between theirs and ours. First, although not presented by them, we find that the delay time of the chosen parameters can be different for different MLT sectors. The observed difference in delays for different MLT sectors may indicate that different mechanisms are responsible for the excitation of waves. More careful analysis of observations will be required in the future to validate this conclusion. Second, we show that the correlation with *AE* inside the plasmapause is unambiguous, while they presented an ambiguous correlation in *AE*, which may indicate that other emissions than magnetosonic waves were included in their data set or they missed it by averaging all of ROCCs over the dayside (6 to 18 MLT). Finally, when modeling the observed waves, they added only one time history of each input instead of including all the relevant times prior to the wave measurements. Our results suggest that it can mislead the accurate evolution of the magnetosonic wave amplitudes. Nevertheless, both studies have confirmed that the southward IMF B_z is the most influential solar wind parameter affecting the variation in dayside wave amplitudes, and the solar wind number density (on behalf of dynamic pressure, which is mostly proportional to the N_{SW} unless V_{SW} is high enough, though it is defined by multiplying N_{SW} by the square of V_{SW}) is responsible mainly for the duskside enhancement. The role of the solar wind number density (or dynamic pressure) outside the plasmapause and solar wind speed inside the plasmapause will be further pursued in the future.

Acknowledgments
This research was supported by Basic Science Research Program through the National Research Foundation of Korea (NRF) funded by the Ministry of Education (NRF-2016R1D1A1B03935148). Y.Y.S. would like to acknowledge funding from the European Union's Horizon 2020 research and innovation program under grant agreement 637302 and Helmholtz Associate ion Rutting Initiative. We thank the GSFC/SPDF OMNIWeb for the provision of the solar wind parameters and geomagnetic activity indices used in this report. The EMFISIS data used for this paper are available from http://emfisis.physics.uiowa.edu/Flight/. We graciously thank the EMFISIS Principal Investigator, Craig Kletzing, and the EMFISIS team.

References

Balikhin, M. A., Y. Y. Shprits, S. N. Walker, L. Chen, N. Cornilleau-Wehrlin, I. Dandouras, O. Santolik, C. Carr, K. H. Yearby, and B. Weiss (2015), Observations of discrete harmonics emerging from equatorial noise, *Nat. Phys.*, doi:10.1038/ncomms8703.

Boardsen, S. A., D. L. Gallagher, D. A. Gurnett, W. K. Peterson, and J. L. Green (1992), Funnel-shaped, low-frequency equatorial waves, *J. Geophys. Res.*, *97*(A10), 14,967–14,976, doi:10.1029/92JA00827.

Chen, L., R. M. Thorne, V. K. Jordanova, and R. B. Horne (2010), Global simulation of magnetosonic wave instability in the storm time magnetosphere, *J. Geophys. Res.*, *115*, A11222, doi:10.1029/2010JA015707.

Chen, L., R. M. Thorne, V. K. Jordanova, M. F. Thomsen, and R. B. Horne (2011), Magnetosonic wave instability analysis for proton ring distributions observed by the LANL magnetospheric plasma analyzer, *J. Geophys. Res.*, *116*, A03223, doi:10.1029/2010JA016068.

Cully, C. M., R. E. Ergun, K. Stevens, A. Nammari, and J. Westfall (2008), The THEMIS digital fields board, *Space Sci. Rev.*, *141*(1–4), 343–355, doi:10.1007/s11214-008-9417-1.

Curtis, S., and C. Wu (1979), Gyroharmonic emissions induced by energetic ions in the equatorial plasmasphere, *J. Geophys. Res.*, *84*(A6), 2597–2607, doi:10.1029/JA084iA06p02597.

Draper, N. R., and H. Smith (1998), *Applied Regression Analysis*, 3rd ed., pp. 20–27, John Wiley, New York.

Horne, R. B., G. V. Wheeler, and H. S. C. K. Alleyne (2000), Proton and electron heating by radially propagating fast magnetosonic waves, *J. Geophys. Res.*, *105*(A12), 27,597–27,610, doi:10.1029/2000JA000018.

Horne, R. B., R. M. Thorne, S. A. Glauert, N. P. Meredith, D. Pokhotelov, and O. Santolík (2007), Electron acceleration in the Van Allen radiation belts by fast magnetosonic waves, *Geophys. Res. Lett.*, *34*, L17107, doi:10.1029/2007GL030267.

Hrbáčková, Z., O. Santolík, F. Němec, E. Macúšová, and N. Cornilleau-Wehrlin (2015), Systematic analysis of occurrence of equatorial noise emissions using 10 years of data from the Cluster mission, *J. Geophys. Res. Space Physics*, *120*, 1007–1021, doi:10.1002/2014JA020268.

Kasahara, Y., H. Kenmochi, and I. Kimura (1994), Propagation characteristics of the ELF emissions observed by the satellite Akebono in the magnetic equatorial region, *Radio Sci.*, *29*, 751–767, doi:10.1029/94RS00445.

Kim, K.-C., and L. Chen (2016), Modeling the storm time behavior of the magnetosonic waves using solar wind parameters, *J. Geophys. Res. Space Physics*, *121*, 446–458, doi:10.1002/2015JA021716.

Laakso, H., H. Junginger, A. Roux, R. Schmidt, and C. deVilledary (1990), Magnetosonic waves above fc (H+) at geostationary orbit: GEOS 2 results, *J. Geophys. Res.*, *95*(A7), 10,609–10,621, doi:10.1029/JA095iA07p10609.

Ma, Q., W. Li, R. M. Thorne, and V. Angelopoulos (2013), Global distribution of equatorial magnetosonic waves observed by THEMIS, *Geophys. Res. Lett.*, *40*, 1895–1901, doi:10.1002/grl.50434.

Ma, Q., W. Li, L. Chen, R. M. Thorne, and V. Angelopoulos (2014), Magnetosonic wave excitation by ion ring distributions in the Earth's inner magnetosphere, *J. Geophys. Res. Space Physics*, *119*, 844–852, doi:10.1002/2013JA019591.

Ma, Q., W. Li, R. M. Thorne, J. Bortnik, C. A. Kletzing, W. S. Kurth, and G. B. Hospodarsky (2016), Electron scattering by magnetosonic waves in the inner magnetosphere, *J. Geophys. Res. Space Physics*, *121*, 274–285, doi:10.1002/2015JA021992.

McIlwain, C. E. (1961), Coordinates for mapping the distribution of magnetically trapped particles, *J. Geophys. Res.*, *66*(11), 3681–3691, doi:10.1029/JZ066i011.

Meredith, N. P., R. B. Horne, R. M. Thorne, D. Summers, and R. R. Anderson (2004), Substorm dependence of plasmaspheric hiss, *J. Geophys. Res.*, *109*, A06209, doi:10.1029/2004JA010387.

Meredith, N. P., R. B. Horne, and R. R. Anderson (2008), Survey of magnetosonic waves and proton ring distributions in the Earth's inner magnetosphere, *J. Geophys. Res.*, *113*, A06213, doi:10.1029/2007JA012975.

Perraut, S., A. Roux, P. Robert, R. Gendrin, J.-A. Sauvaud, J.-M. Bosqued, G. Kremser, and A. Korth (1982), A systematic study of ULF waves above FH+ from GEOS 1 and 2 measurements and their relationships with proton ring distributions, *J. Geophys. Res.*, *87*(A8), 6219–6236, doi:10.1029/JA087iA08p06219.

Press, W. H., S. A. Teukolsky, W. T. Betterling, and B. P. Flannery (1992), *Numerical Recipes in C: The Art of Scientific Computing*, pp. 640–642, Cambridge Univ. Press, New York.

Russell, C. T., R. E. Holzer, and E. J. Smith (1970), OGO 3 observations of ELF noise in the magnetosphere: 2. The nature of the equatorial noise, *J. Geophys. Res.*, *75*(4), 755–768, doi:10.1029/JA075i004p00755.

Santolík, O., J. S. Pickett, D. A. Gurnett, M. Maksimovic, and N. Cornilleau-Wehrlin (2002), Spatiotemporal variability and propagation of equatorial noise observed by Cluster, *J. Geophys. Res.*, *107*(A12), 1495, doi:10.1029/2001JA009159.

Santolík, O., M. Parrot, and F. Lefeuvre (2003), Singular value decomposition methods for wave propagation analysis, *Radio Sci.*, *38*(1), 1010, doi:10.1029/2000RS002523.

Santolík, O., F. Nemec, K. Gereova, E. Macusova, Y. de Conchy, and N. Cornilleau-Wehrlin (2004), Systematic analysis of equatorial noise below the lower hybrid frequency, *Ann. Geophys.*, *22*, 2587–2595.

Shprits, Y. Y. (2016), Estimation of bounce resonant scattering by fast magnetosonic waves, *Geophys. Res. Lett.*, *43*, 998–1006, doi:10.1002/2015GL066796.

Shprits, Y. Y., A. Runov, and B. Ni (2013), Gyro-resonant scattering of radiation belt electrons during the solar minimum by fast magnetosonic waves, *J. Geophys. Res. Space Physics*, *118*, 648–652, doi:10.1002/jgra.50108.

Stix, T. H. (1992), *Waves in Plasmas*, pp. 3–12, Springer, New York.

Tsurutani, B. T., B. J. Falkowski, J. S. Pickett, O. P. Verkhoglyadova, O. Santolík, and G. S. Lakhina (2014), Extremely intense ELF magnetosonic waves: A survey of polar observations, *J. Geophys. Res. Space Physics*, *119*, 964–977, doi:10.1002/2013JA019284.

Tsyganenko, N. A., and M. I. Sitnov (2005), Modeling the dynamics of the inner magnetosphere during strong geomagnetic storms, *J. Geophys. Res.*, *110*, A03208, doi:10.1029/2004JA010798.

Xiao, F., Q. Zong, Y. Wang, Z. He, Z. Su, C. Yang, and Q. Zhou (2014), Generation of proton aurora by magnetosonic waves, *Sci. Rep.*, *4*, 5190, doi:10.1038/srep05190.

Zhima, Z., L. Chen, H. Fu, J. Cao, R. B. Horne, and G. Reeves (2015), Observations of discrete magnetosonic waves off the magnetic equator, *Geophys. Res. Lett.*, *42*, 9694–9701, doi:10.1002/2015GL066255.